Ramesh, K., Gopalarathnam, A., Edwards, J.R., Granlund, K., and Ol, M.V. (2013) Theoretical analysis of perching and hovering maneuvers. In: 43rd AIAA Fluid Dynamics Conference and Exhibit, 24-27 Jun 2013, San Diego, CA, USA.

http://eprints.gla.ac.uk/99368

Deposited on: 25 November 2014

Theoretical Analysis of Perching and Hovering Maneuvers

Kiran Ramesh,[*] Ashok Gopalarathnam,[†] Jack R.Edwards[‡]

Department of Mechanical and Aerospace Engineering,
North Carolina State University, Raleigh, NC 27695-7910

Kenneth Granlund[§] Michael V. Ol[¶]

U.S. Air Force Research Laboratory, Air Vehicles Directorate,
AFRL/RBAA, Bldg. 45, 2130 8th St., WPAFB, OH 45433-7542

Unsteady aerodynamic phenomena are encountered in a large number of modern aerospace and non-aerospace applications. Leading edge vortices (LEVs) are of particular interest because of their large impact on the forces and performance. In rotorcraft applications, they cause large vibrations and torsional loads (dynamic stall), affecting the performance adversely. In insect flight however, they contribute positively by enabling high-lift flight. Identifying the conditions that result in LEV formation and modeling their effects on the flow is an important ongoing challenge. Perching (airfoil decelerates to rest) and hovering (zero freestream velocity) maneuvers are of special interest. In earlier work by the authors, a Leading Edge Suction Parameter (LESP) was developed to predict LEV formation for airfoils undergoing arbitrary variation in pitch and plunge at a constant freestream velocity. In this research, the LESP criterion is extended to situations where the freestream velocity is varying or zero. A point-vortex model based on this criterion is developed and results from the model are compared against those from a computational fluid dynamics (CFD) method. Abstractions of perching and hovering maneuvers are used to validate the low-order model's performance in highly unsteady vortex-dominated flows, where the time-varying freestream/translational velocity is small in magnitude compared to the other contributions to the velocity experienced by the leading edge region of the airfoil. Time instants of LEV formation, flow topologies and force coefficient histories for the various motion kinematics from the low-order model and CFD are obtained and compared. The LESP criterion is seen to be successful in predicting the start of LEV formation and the point-vortex method is effective in modeling the flow development and forces on the airfoil. Typical run-times for the low-order method are between 30–40 seconds, making it a potentially convenient tool for control/design applications.

Nomenclature

α	pitch angle, angle of airfoil chord with inertial horizontal
$\dot{\alpha}$	pitch rate
$\dot{h}$	plunge rate
$\eta(x)$	variation of camber along airfoil
$\gamma(x,t)$	chordwise vorticity distribution
Γ_{b_t}	bound circulation of airfoil at time t
Γ_{lev_n}	strength of nth leading edge vortex

[*]Graduate Research Assistant, Box 7910, kramesh2@ncsu.edu, (919) 600-0519. Student Member, AIAA

[†]Associate Professor, Box 7910, ashok_g@ncsu.edu, (919) 515-5669. Associate Fellow, AIAA

[‡]Professor, Box 7910, jredward@ncsu.edu, (919) 515-5264. Associate Fellow, AIAA

[§]Post-Doctoral Scholar, kenneth.granlund@WPAFB.AF.MIL, Member,AIAA

[¶]Aerospace Engineer, Michael.Ol@WPAFB.AF.MIL, Associate Fellow, AIAA

Γ_{tev_m}	strength of mth trailing edge vortex
ϕ_B	velocity potential from bound circulation
ϕ_{lev}	velocity potential from leading edge vortices
ϕ_l	lower surface velocity potential
ϕ_{tev}	velocity potential from trailing edge vortices
ϕ_u	upper surface velocity potential
ρ	fluid density
θ	variable of transformation of chordwise distance
a	pivot location on the airfoil from 0 to 1 (x/c)
$A_0, A_1, A_2....$	Fourier coefficients
$Bxyz$	body frame
c	airfoil chord
C_d	drag coefficient
C_l	lift coefficient
C_m	pitching moment coefficient
C_N	normal force coefficient
C_S	leading edge suction force coefficient
cm_{pvt}	pivot for pitching moment calculation
F_N	normal force on airfoil
F_S	leading edge suction force on airfoil
h	plunge displacement
M	moment on airfoil
$OXYZ$	inertial frame
$p(x)$	pressure on airfoil surface
Re_{ref}	Reynolds number based on reference velocity
$Re_{V_{mag}}$	Reynolds number based on resultant velocity at the leading edge
S	suction at the leading edge
t	time
t^*	nondimensional time $= \frac{tU_{ref}}{c}$
$U(t)$	time-varying freestream velocity
U_{ref}	reference velocity
V_t	tangential velocity on airfoil surface
V_{mag}	magnitude of resultant velocity at the leading edge
$W(x,t)$	local downwash
x	chordwise distance
x_p	reference for pitching moment calculation
LESP	leading edge suction parameter

I.   Introduction

Interest in understanding the capabilities of natural flyers such as birds, bats and insects, and in developing micro air vehicles (MAVs) has resulted in substantial research efforts toward flapping flight and the underlying unsteady aerodynamics. Perching maneuvers (employed by birds while landing) and hovering maneuvers (exhibited by several insects) are of special interest. Perching can be modeled as a ramp variation in angle of attack, in conjunction with the freestream velocity decreasing to zero (during landing). Hovering maneuvers involve zero freestream and translational velocity. Some recent computational and experimental studies on these motions can be found in Refs. 1–5.

Perching and hovering maneuvers are hence special cases of a more general set of kinematics involving variable freestream velocity. Classical unsteady theories, such as those by Theodorsen,[6] Wagner[7] and von Kármán and Sears[8] solve the unsteady two-dimensional flow problem assuming small amplitudes, planar wakes and constant freestream velocity. Isaacs[9] assumed the freestream velocity to be a constant plus a sinusoidal term and derived a solution for the lift on the airfoil. Greenberg[10] developed an extension to Theodorsen's theory which modeled non-constant freestream, assuming that the wake was sinusoidal. A method to solve for the loads on an airfoil in an arbitrarily varying freestream using an indicial response is

given by van der Wall and Leishman.[11]

Unsteady aerodynamic phenomena are also encountered in dynamic stall in rotors. A common characteristic between rotorcraft dynamic stall and insect/MAV aerodynamics is the presence of the Leading Edge Vortex (LEV). LEV formation in rotorcraft and the accompanying dynamic stall phenomena are usually detrimental to performance of the vehicle.[12] On the other hand, LEVs are credited with being largely responsible for the success of high-lift flight in insects.[13–16] For both scenarios, the identification of conditions resulting in LEV formation is an important challenge.

Low-order numerical models based on point vortex methods are useful tools in studying unsteady aerodynamics. While the computational cost may be kept low in comparison with a conventional CFD method, unsteady phenomena such as flow separation may be modeled using phenomenological augmentation of the method. Sarpkaya,[17]Katz[18] and Clements[19] are some of the researchers who have applied point vortex methods to unsteady scenarios such as separated flow on an airfoil and bluff body flow. An extensive review of the literature in vortex methods up to the 1980s is given by Leonard.[20] More recently, Ansari et al.,[21] Pullin & Wang[22] and Wang & Eldredge[23] have proposed point vortex methods to model the effects the leading edge vortices on the flowfield and forces. However, a common drawback in all these methods is that the conditions under which flow separation occur are not defined. Instead, it is assumed that the flow is always separated at the leading edge and a Kutta condition is enforced at the leading edge at all times. While this assumption is valid for flat plates with sharp leading edges, rounded airfoils can support a certain amount of suction at the leading edge. Hemati et al.[24] have recently employed optimum control theory to establish that relaxing the Kutta condition at the leading edge improves model predictions in comparison with high-fidelity methods. Hence a criterion to identify flow separation at the leading edge is necessary to accurately model LEVs using point vortex methods.

In previous work, the authors developed an unsteady airfoil theory which accounted for large amplitudes and nonplanar wakes,[25] and proposed the Leading Edge Suction Parameter (LESP) criterion[26] to predict the onset of LEV formation. For a given Reynolds number and airfoil, it was shown that LEV formation is always initiated at the same value of LESP (calculated from inviscid theory), regardless of motion kinematics. This criterion was used in conjunction with the unsteady airfoil theory to develop a point vortex method with LESP-modulated vortex shedding from the leading edge.[27] The results from this model were successfully validated against flow visualization and force histories from experimental and computational data. In the current research, we aim to extend the low-order model to situations involving arbitrary variation in translational/freestream velocity. Hence, the LESP hypothesis is generalized to account for variation in Reynolds number during the motion. A point-vortex model is developed, using the revised LESP hypothesis to modulate vortex shedding at the leading edge.

II.   Theoretical Formulation

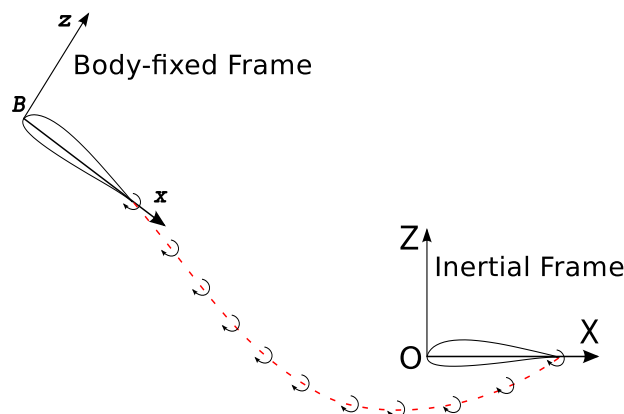### II.A.   Time stepping approach

Figure 1. An illustration of the time stepping method.

Details of this time stepping method can be found in Refs. 25 and 28. The inertial frame is given by $OXYZ$ and the body frame attached to the airfoil is given by $Bxyz$. At time $t = 0$, the body frame is assumed to coincide with the inertial frame and at time $t > 0$, moves towards the left of the page along a prescribed path. At each discrete time-step, a trailing-edge vortex is shed from the trailing-edge as shown in Figure 1. Leading edge vortices are shed in accordance with the LESP criterion which is detailed in Section II.C.

The vorticity distribution over the airfoil is taken to be a Fourier series in a manner analogous to thin-airfoil theory.

$$\gamma(\theta, t) = 2V_{mag}(t) \left[A_0(t) \frac{1 + \cos\theta}{\sin\theta} + \sum_{n=1}^{\infty} A_n(t) sin(n\theta) \right] \tag{1}$$

where,

$$x = \frac{1}{2}(1 - \cos\theta) \tag{2}$$

θ varies from 0 to π as x varies from 0 to 1 along the airfoil. V_{mag} is the magnitude of resultant velocity at the leading edge, derived as a function of airfoil motion, freestream and induced velocities by free vortices (Figure 2). The location of pitch pivot is given by a and V_{ind} is calculated as described in Section II.D.

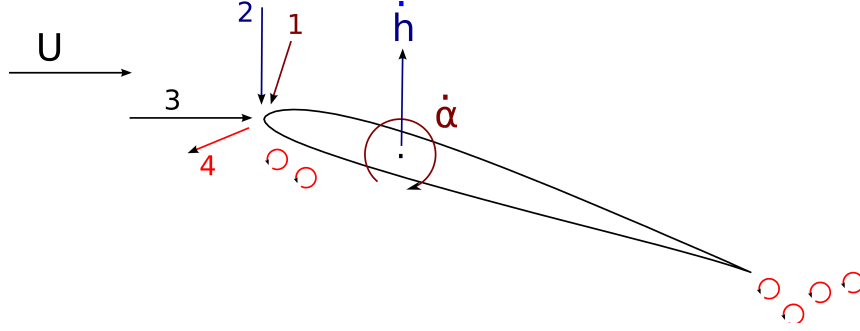$$V_{mag} = |\vec{U} + \vec{\dot{h}} + \vec{\dot{\alpha}}ac + \vec{V_{ind}}| \tag{3}$$

Figure 2. 1, 2, 3 and 4 are the flow velocity contributions at the LE due to $\dot{\alpha}$, $\dot{h}$, U and vortical structures respectively. The magnitude of their vector sum is V_{mag}.

We note that in our earlier work,[25–27] the instantaneous freestream velocity $U(t)$ was used instead of v_{mag} in Eqn. 1. In the current paper, since the method is extended to cases where $U(t)$ can become zero or small compared to the other perching or hovering velocity contributions, $V_{mag}(t)$ has been used as the better scaling parameter in Eqn. 1.

II.B. Calculation of local downwash and Fourier coefficients

The Fourier coefficients are given in terms of the local downwash $W(x,t)$ as:

$$A_0(t) = -\frac{1}{\pi} \int_0^\pi \frac{W(x,t)}{V_{mag}(t)} d\theta \tag{4}$$

$$A_n(t) = \frac{2}{\pi} \int_0^\pi \frac{W(x,t)}{V_{mag}(t)} \cos n\theta d\theta \tag{5}$$

The local downwash is calculated by enforcing the boundary condition of zero normal flow on the airfoil surface:

$$W(x,t) \equiv \frac{\partial \phi_B}{\partial z} = \frac{\partial \eta}{\partial x} \left[U(t)\cos\alpha + \dot{h}\sin\alpha + \frac{\partial \phi_{lev}}{\partial x} + \frac{\partial \phi_{tev}}{\partial x} \right] - U(t)\sin\alpha - \dot{\alpha}(x - ac) + \dot{h}\cos\alpha - \frac{\partial \phi_{tev}}{\partial z} - \frac{\partial \phi_{lev}}{\partial z} \tag{6}$$

where $\frac{\partial \phi_{lev}}{\partial x}$ and $\frac{\partial \phi_{tev}}{\partial x}$ are velocities induced along the chord and $\frac{\partial \phi_{lev}}{\partial z}$ and $\frac{\partial \phi_{tev}}{\partial z}$ are the induced velocities normal to the chord due to discrete vortices in the flow shed by the leading and trailing edges. The calculation of these quantities is detailed in section II.D.

The unknown at each time step is the strength of the last shed trailing edge vortex, assuming that no leading edge vortex is formed at this time step. This is calculated iteratively using a Newton-Raphson iteration to satisfy Kelvin's condition.

$$\Gamma_{b_t} + \sum_{m=1}^{n_{tev}} \Gamma_{tev_m} + \sum_{n=1}^{n_{lev}} \Gamma_{lev_n} = 0 \tag{7}$$

where Γ_{b_t} is the bound circulation calculated by integrating the chordwise vorticity over the airfoil chord:

$$\Gamma_{b_t} = V_{mag}(t)c\pi \left[A_0(t) + \frac{A_1(t)}{2} \right] \tag{8}$$

II.C.   Criterion for prediction of LEV formation using LESP

The Leading Edge Suction Parameter (LESP)[26] is a measure of the suction peak at the leading edge, which in turn is caused by the stagnation point moving away from the leading edge when the airfoil is at an angle of attack. As the airfoil thickness approaches zero, the leading edge radius also approaches zero giving rise to a theoretically infinite flow velocity at the leading edge. From Refs. 29 and 30, we have that the form of the infinity is:

$$V_{LE}(t) = \lim_{x \to LE} \frac{S}{\sqrt{x}} \tag{9}$$

S is a measure of the suction at the leading edge and is given by,

$$S = \lim_{x \to LE} \frac{1}{2} \gamma(x,t) \sqrt{x} \tag{10}$$

Since $\gamma(x,t)$ is infinite in order of $1/\sqrt{x}$ at the leading edge, the value of S is finite. Evaluating using the current formulation,

$$S = \sqrt{c} V_{mag}(t) A_0(t) \tag{11}$$

Although the theoretical velocity at the leading edge is infinite, real airfoils have rounded leading edges which can support some suction even when the stagnation point is away from the leading edge.[18] The amount of suction that can be supported is a characteristic of the airfoil shape and Reynolds number of operation. In previous research,[26] the Leading Edge Suction Parameter was defined as the quantity obtained by nondimensionalizing the suction with a function of the reference velocity ($LESP(t) = A_0(t)$). Following the lines of work by Evans & Mort[31] and Beddoes[32] who observed that LEV formation was correlated with the occurrence of critical value of velocity/pressure gradient peak at the leading edge, we hypothesized that LEV formation is correlated with a critical value of the LESP. Using dye-flow images from experiment and vorticity plots from computation, we verified that LEV formation occurred at a critical value of LESP, irrespective of motion kinematics as long as the airfoil and freestream Reynolds number remained the same.

In the current research, the freestream velocity is time variant and can become zero or small compared to other velocity contributions. For the purpose of characterizing flow at the leading edge, specifically the boundary layer development and separation leading to LEV formation, a better Reynolds number is one that is based on $V_{mag}(t)$ instead of $U(t)$. We refer to this Reynolds number as $Re_{V_{mag}}$:

$$Re_{V_{mag}}(t) = \frac{V_{mag}(t)c}{\nu} \tag{12}$$

$$= \frac{V_{mag}(t)}{U_{ref}} Re_{ref} \tag{13}$$

where Re_{ref} is Reynolds number based on reference velocity ($Re_{ref} = \frac{U_{ref}c}{\nu}$).

American Institute of Aeronautics and Astronautics

The LESP is defined as the quantity obtained by nondimensionalizing the leading edge suction by $\sqrt{c}V_{mag}$:

$$LESP(t) = A_0(t) \tag{14}$$

Using data from experiment or CFD, the critical LESP value must be calibrated over a range of $Re_{V_{mag}}$ values. During the motion, the critical LESP value is calculated as a function of the leading edge Reynolds number and is used to identify LEV formation. If the instantaneous absolute value of LESP is higher than the instantaneous critical value, vortices are shed from the leading edge. The sign of the LESP indicates the surface of LEV formation - positive for airfoil upper surface and negative for the lower surface.

It is noted here that is LESP criterion is not derived on rigorous mathematical proof. The hypothesis is based on physical reasoning along the lines of work by Evans & Mort[31] and Beddoes.[32] The definition of LESP and the choice of calibrating it with the leading edge Reynolds number arise from physical arguments and validation of several scenarios against results from CFD. Results for verification of the LESP hypothesis are presented in Section III.B.

II.D. Modeling of vortex shedding using LESP

In the point-vortex model presented in this paper, vortices are shed from the trailing-edge at every time instant. At the leading-edge however, vortices are shed only at instants when the LESP is greater than the $LESP_{crit}$. The strength of the shed vortex at the leading edge is determined by iteration such that the instantaneous LESP is brought back to the instantaneous critical LESP value. This models the expected behavior that rounded leading edges support a certain amount of suction even when the flow is separated.[18, 24]

In the current model, the vortex placement methodology given by Ansari *et al.*[21, 33] is used, where the latest vortex is placed at one-third of the distance from the shedding edge to the previous shed vortex.

$$(x, z)_{tev_i/lev_i} = (x, z)_{TE/LE} + \frac{1}{3}((x, z)_{tev_{i-1}/lev_{i-1}} - (x, z)_{TE/LE}) \tag{15}$$

The position of first shed vortex at the leading edge is calculated as a function of the velocity at the leading edge. Note that trailing edge vortices are shed at every time step but leading edge vortices are shed only when the LESP is in excess of the critical value. In this model, the newest vortices are placed as a function of the velocity at the leading edge (V_{mag}) at that instant.

Traditionally, the Biot-Savart law is used to calculate the velocities induced by point vortices at other points in the field. However, using a singular vortex model leads to very high induced velocities when the distance between vortices is small. Here, the vortex model proposed by Vatistas et al.[34] is used, which gives a very good approximation to the Lamb-Oseen vortex. Using Vatistas vortex model with order 2, we have that the velocities induced by the kth vortex in the X and Z directions (u and w) are :

$$u = \frac{\gamma_k}{2\pi} \frac{z - z_k}{\sqrt{((x - x_k)^2 + (z - z_k)^2)^2 + v_{core}^4}} \tag{16}$$

$$w = -\frac{\gamma_k}{2\pi} \frac{x - x_k}{\sqrt{((x - x_k)^2 + (z - z_k)^2)^2 + v_{core}^4}} \tag{17}$$

All leading edge and trailing edge vortices are convected with the local velocity at their positions, at each time step. The local velocity at the vortex locations includes contributions from bound, leading edge and trailing edge vortices.

II.E. Pressure distribution and forces on airfoil

Using the unsteady Bernoulli's theorem and thin airfoil theory relations, we have:

$$\Delta p(x) = p_l(x) - p_u(x) \tag{18}$$

$$= \rho \left(\frac{1}{2}(V_{t_u}^2 - V_{t_l}^2) + \left(\frac{\partial \phi}{\partial t} \right)_u - \left(\frac{\partial \phi}{\partial t} \right)_l \right) \tag{19}$$

$$\phi = \phi_b + \phi_{lev} + \phi_{tev} \tag{20}$$

American Institute of Aeronautics and Astronautics

$$V_{t_u} = U(t)\cos\alpha + \dot{h}\sin\alpha + \left(\frac{\partial\phi_{lev}}{\partial x}\right)_u + \left(\frac{\partial\phi_{tev}}{\partial x}\right)_u + \left(\frac{\partial\phi_b}{\partial x}\right)_u \tag{21}$$

$$V_{t_l} = U(t)\cos\alpha + \dot{h}\sin\alpha + \left(\frac{\partial\phi_{lev}}{\partial x}\right)_l + \left(\frac{\partial\phi_{tev}}{\partial x}\right)_l + \left(\frac{\partial\phi_b}{\partial x}\right)_l \tag{22}$$

$$\tag{23}$$

Drawing from thin airfoil theory:

$$\left(\frac{\partial\phi_b}{\partial x}\right)_u = \frac{\gamma(x)}{2} \tag{24}$$

$$\left(\frac{\partial\phi_b}{\partial x}\right)_l = -\frac{\gamma(x)}{2} \tag{25}$$

$$V_{t_u}^2 - V_{t_l}^2 = 2\left(U(t)\cos\alpha + \dot{h}\sin\alpha + \left(\frac{\partial\phi_{lev}}{\partial x}\right) + \left(\frac{\partial\phi_{tev}}{\partial x}\right)\right)\gamma(x) \tag{26}$$

$$\phi_u = \int_0^x \frac{\gamma(x)}{2}dx + \int_0^x \left(\frac{\partial\phi_{lev}}{\partial x}\right)dx + \int_0^x \left(\frac{\partial\phi_{tev}}{\partial x}\right)dx \tag{27}$$

$$\phi_l = -\int_0^x \frac{\gamma(x)}{2}dx + \int_0^x \left(\frac{\partial\phi_{lev}}{\partial x}\right)dx + \int_0^x \left(\frac{\partial\phi_{tev}}{\partial x}\right)dx \tag{28}$$

$$\left(\frac{\partial\phi}{\partial t}\right)_u - \left(\frac{\partial\phi}{\partial t}\right)_l = \frac{\partial}{\partial t}\int_0^x \gamma(x)dx \tag{29}$$

From equations 19, 26 and 29,

$$\Delta p(x) = \rho\left(U(t)\cos\alpha + \dot{h}\sin\alpha + \left(\frac{\partial\phi_{lev}}{\partial x}\right) + \left(\frac{\partial\phi_{tev}}{\partial x}\right)\right)\gamma(x) + \frac{\partial}{\partial t}\int_0^x \gamma(x)dx \tag{30}$$

The first term is similar to the steady-state circulatory term and the second is the contribution of time dependency/fluid acceleration. The normal force on the airfoil is obtained by integrating the pressure distribution over the airfoil chord.

$$F_N = \rho\pi c V_{mag}\left[\left(U(t)\cos\alpha + \dot{h}\sin\alpha + \left(\frac{\partial\phi_{lev}}{\partial x}\right) + \left(\frac{\partial\phi_{tev}}{\partial x}\right)\right)\left(A_0 + \frac{A_1}{2}\right) + c\left(\frac{3\dot{A}_0}{4} + \frac{\dot{A}_1}{4} + \frac{\dot{A}_2}{8}\right)\right] \tag{31}$$

In addition to the normal force, there is a leading edge suction force acting axial to the airfoil, given by the Blasius formula. Employing the current formulation gives:

$$F_S = \rho\pi c V_{mag}^2 A_0^2 \tag{32}$$

The non-dimensional force coefficients are obtained by dividing the forces with $\frac{1}{2}\rho U_{ref}^2 c$. The lift and drag coefficients are comprised of components from the normal and leading edge suction forces:

$$C_l = C_N\cos\alpha + C_S\sin\alpha \tag{33}$$

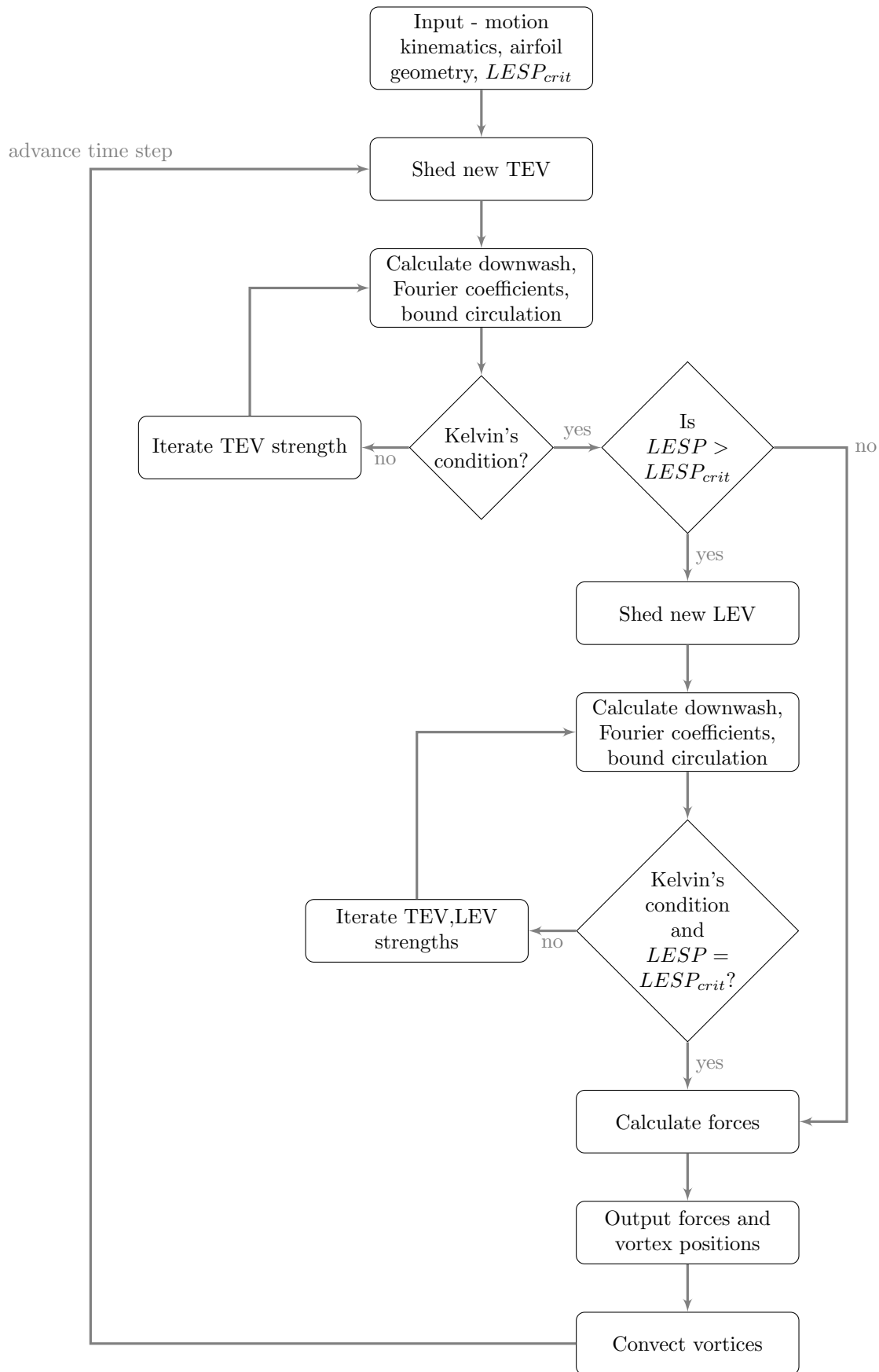$$C_d = C_N\sin\alpha - C_S\cos\alpha \tag{34}$$

The pitching moment coefficient of the airfoil, about a reference x_p is given by:

$$M = \int_0^c \Delta p(x)(x - x_p)dx \tag{35}$$

$$C_m = \frac{M}{\frac{1}{2}\rho U_{ref}^2 c^2} \tag{36}$$

II.F.   Summary of model - Flowchart

American Institute of Aeronautics and Astronautics

III. Results

III.A. Use of CFD for calibration and verification

The LESP hypothesis is verified using data from CFD. The CFD calculations presented in this work were performed using NCSU's REACTMB-INS code, which solves the time-dependent incompressible Navier-Stokes equations using a finite-volume method. The governing equations are written in arbitrary Lagrangian / Eulerian (ALE) form, which enables the motion of a body-fitted computational mesh in accord with prescribed rate laws. Spatial discretization of the inviscid fluxes uses a low-diffusion flux-splitting method valid in the incompressible limit.[35] The Spalart-Allmaras model[36] as implemented by Edwards and Chandra,[37] is used for turbulence closure. The computations were performed on a 2-D body-fitted mesh containing $92,400$ cells and an SD7003 airfoil is used for all motion kinematics. The scale for all vorticity contour plots shown in this paper is given in Figure 3.
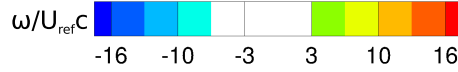
Figure 3. Scale for all vorticity contour plots from CFD.

III.A.1. Calibration of $LESP_{crit}$ with $Re_{V_{mag}}$

To calibrate the $LESP_{crit}$ against $Re_{V_{mag}}$ for an SD7003 airfoil, LEV shedding must be studied using CFD over a broad range of Reynolds numbers. A pitch-ramp motion to 90 deg is used as a calibration motion. By studying LEV formation for this motion at several Reynolds numbers using CFD, the $LESP_{crit}$ vs Re variation may be determined. This variation was documented in Ref. 38. For this motion, we also know the variation of $Re_{V_{mag}}$ with t^* for an given Re_{ref}. Thus the variation of $LESP_{crit}$ vs Re can be converted to a variation of $LESP_{crit}$ vs $Re_{V_{mag}}$. The angle of attack and LESP variation from theory during this motion are shown in Figure 4. Since we are only examining the results until the point of LEV formation, the LEV shedding in the theoretical model is "turned off". It is noted that the LESP variation is the same for a given motion irrespective of Reynolds number since the theoretical model with no LEV shedding is inviscid.
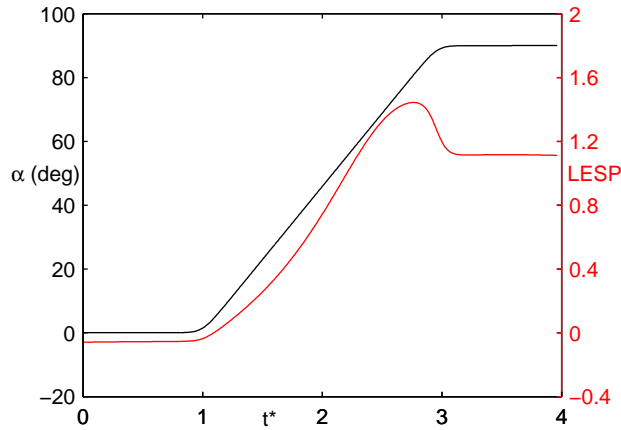

Figure 4. Variation of angle of attack and inviscid LESP for the calibration motion.

The CFD runs were performed at reference Reynolds numbers (Re_{ref} ranging between $1,000$ and $1,000,000$. An SD7003 airfoil was used for all cases. For each run, the time instant of LEV formation was determined from skin-friction coefficient and vorticity plots (identification of LEV formation using skin-friction coefficient from CFD is detailed in the appendix). The LESP value at the time instant of separation

is the critical LESP for the $Re_{V_{mag}}$ at that time. The calibrated values of $LESP_{crit}$ against a log scale of $Re_{V_{mag}}$ are shown in Figure 5.
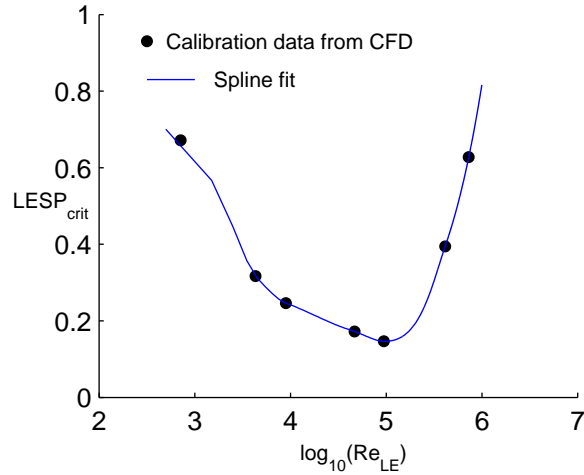

Figure 5. $LESP_{crit}$ **variation with** $Re_{V_{mag}}$ **shown on a log scale.**

III.B. Verification of LESP hypothesis for LEV formation

III.B.1. Perching maneuvers

Perching maneuvers may be approximated using the classical pitch-ramp motion,[5] where the angle of attack varies rapidly over a large amplitude. The key difference between classical ramp motions and perching is that the latter also involves a deceleration to zero freestream velocity. Three perching maneuvers are investigated in this section — pitch-ramp motions with freestream velocity decelerating to zero at different rates with a starting freestream velocity U_{ref} that corresponds to $Re_{ref} = 200,000$. The motion kinematics of these maneuvers are depicted in Figure 6. For each motion, the instantaneous LESP (calculated using theory with LEV Shedding "turned off") and the critical LESP (determined using calibration in Section III.A.1) are co-plotted. The time at intersection of these two curves is the theoretical prediction for instant of LEV formation using the LESP criterion. The time at start of LEV formation is also independently determined using CFD (procedure detailed in appendix) and marked on the plot. Figures 7, 8 and 9 show the comparison between theoretical and computational identification of LEV formation. Vorticity plots from CFD are shown at four instants around the time of LEV formation (at right of figures).
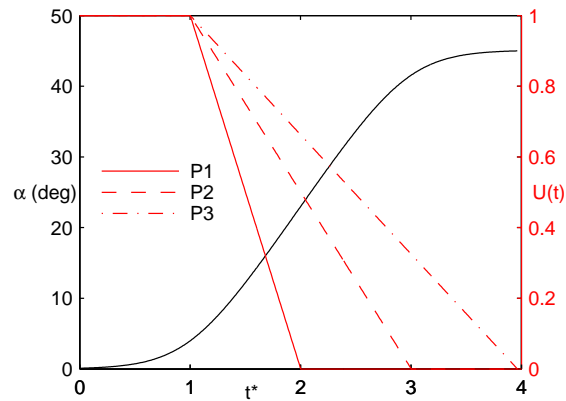
Figure 6. Variation of pitch angle, α, and freestream velocity for perching motions.
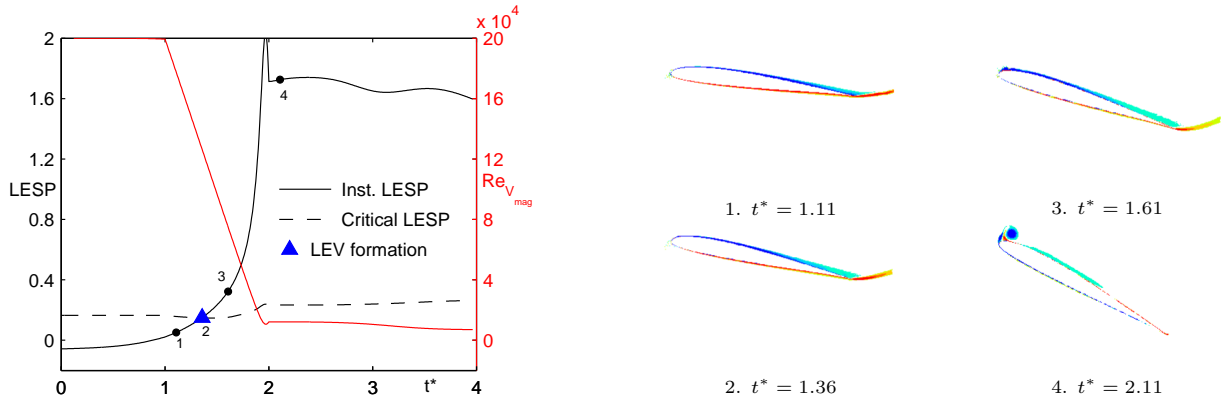
Figure 7. Case P1. Left: Identification of LEV formation using LESP criterion and CFD. The intersection of LESP and critical LESP curves marks the theoretical prediction for start of LEV formation. The prediction from CFD is marked as a triangle. Right: Vorticity plots from CFD at the 4 instants marked on the left figure.
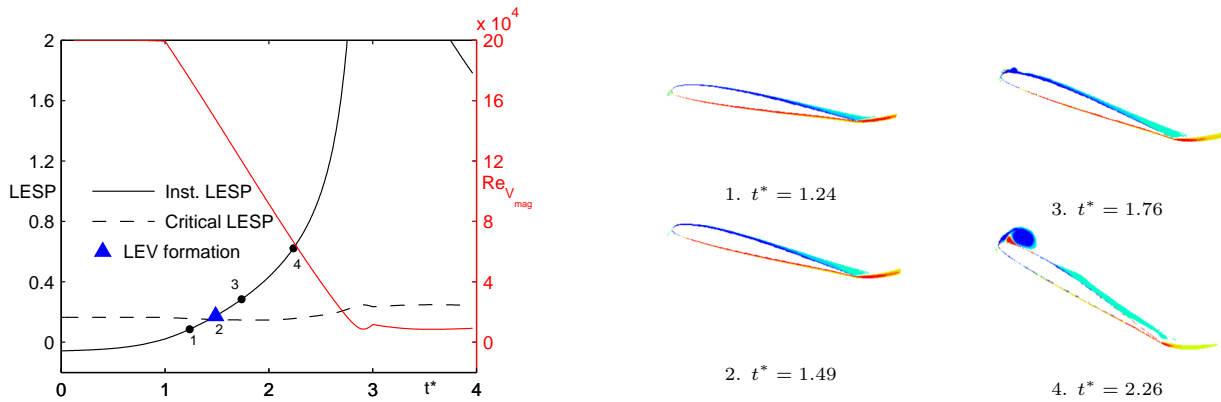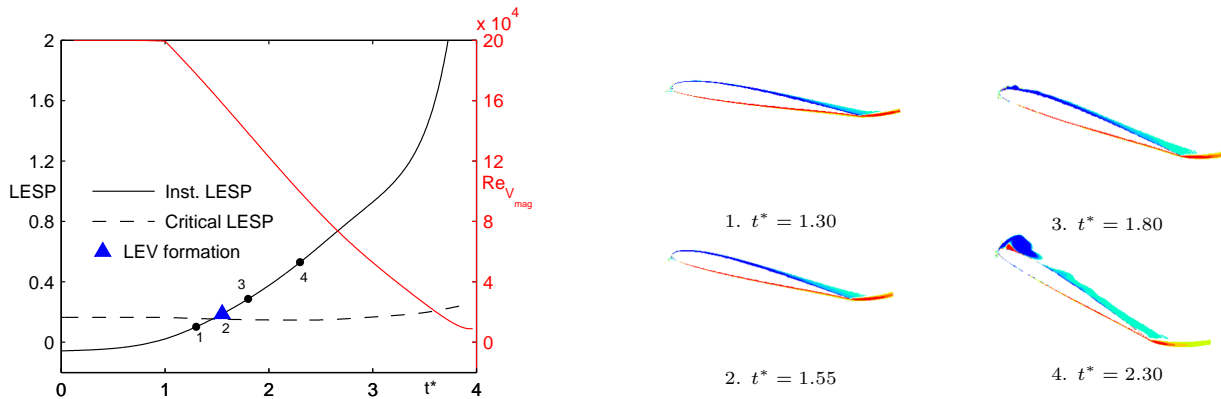

Figure 8. Case P2. Left: Identification of LEV formation using LESP criterion and CFD. The intersection of LESP and critical LESP curves marks the theoretical prediction for start of LEV formation. The prediction from CFD is marked as a triangle. Right: Vorticity plots from CFD at the 4 instants marked on the left figure.

Figure 9. Case P3. Left: Identification of LEV formation using LESP criterion and CFD. The intersection of LESP and critical LESP curves marks the theoretical prediction for start of LEV formation. The prediction from CFD is marked as a triangle. Right: Vorticity plots from CFD at the 4 instants marked on the left figure.

III.B.2. *Hovering maneuvers*

Hovering maneuvers typically involve periodic changes in pitch/plunge at zero freestream/translational velocity. Since we are primarily interested in identification of LEV formation, a single ramp variation in plunge

at zero freestream velocity is used as an abstraction of hovering in this section. Three maneuvers consisting of plunge-ramps at varying static pitch angles (20°, 45°, 60°) and $Re_{ref} = 10,000$ are investigated. Figure 10 shows the motion kinematics of the the three hovering motions.
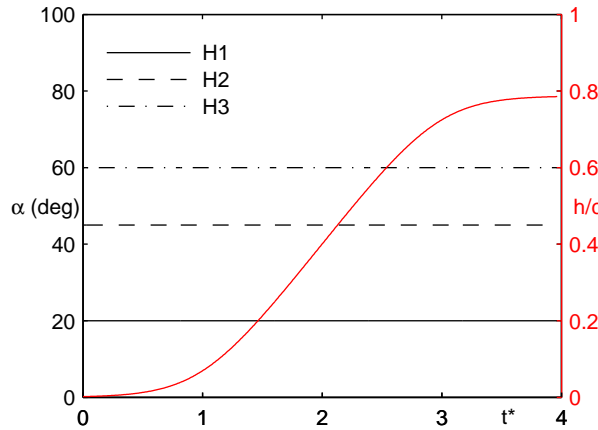

Figure 10. Variation of pitch angles, α, and plunge displacement for hovering motions ($U(t) = 0$).

Figures 11, 12 and 13 depict the identification of LEV formation for the hovering motions using theoretical and computational methods. The absolute value of instantaneous LESP exceeding the critical LESP marks the start of LEV formation from theory. It is noted that for all three cases, the LESP value goes below the negative of critical LESP value, corresponding to lower surface LEV formation.
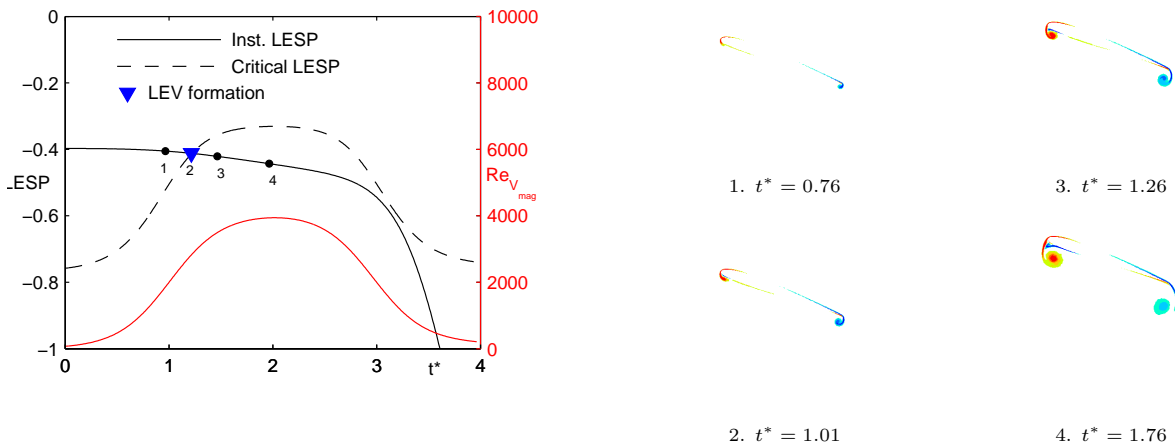
Figure 11. Case H1. Left: Identification of LEV formation using LESP criterion and CFD. The intersection of LESP and critical LESP curves marks the theoretical prediction for start of LEV formation. The prediction from CFD is marked as a triangle. Right: Vorticity plots from CFD at the 4 instants marked on the left figure.

The predictions for LEV formation from theory are seen to compare well with predictions from CFD. The LESP hypothesis, which states that LEV formation occurs when the LESP exceeds a critical value, is successfully verified for cases with varying and zero freestream velocity. We note that the $LESP_{crit}$ vs $Re_{V_{mag}}$ curve is constructed using a spline interpolation of a few points. More data points may hence provide better accuracy of the theory with respect to CFD.
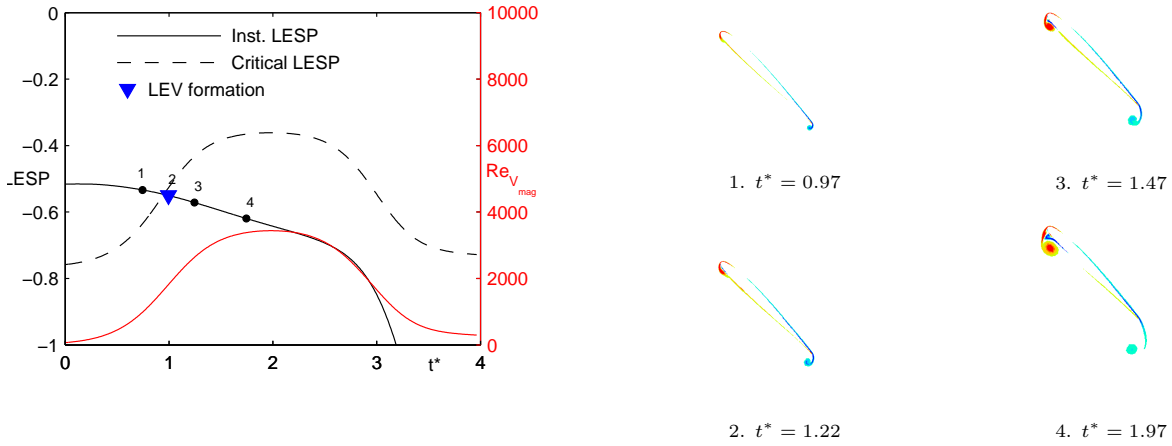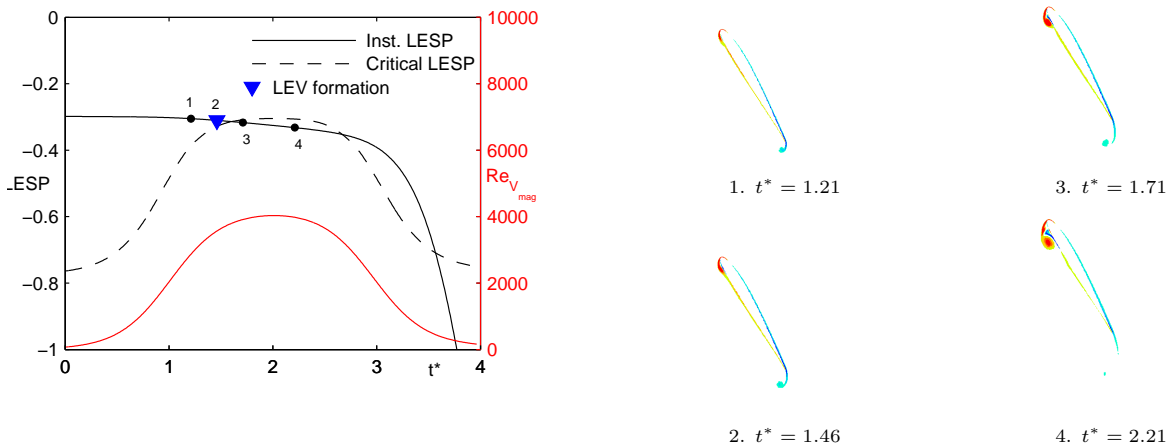
American Institute of Aeronautics and Astronautics

Figure 12. Case H2. Left: Identification of LEV formation using LESP criterion and CFD. The intersection of LESP and critical LESP curves marks the theoretical prediction for start of LEV formation. The prediction from CFD is marked as a triangle. Right: Vorticity plots from CFD at the 4 instants marked on the left figure.

Figure 13. Case H3. Left: Identification of LEV formation using LESP criterion and CFD. The intersection of LESP and critical LESP curves marks the theoretical prediction for start of LEV formation. The prediction from CFD is marked as a triangle. Right: Vorticity plots from CFD at the 4 instants marked on the left figure.

III.C.   Verification of LEV shedding model for flow and force prediction

The discrete vortex model with LESP modulated LEV shedding is used to generate flow topology and force coefficient from theory. At each time instant, the $Re_{V_{mag}}$ value is used to obtain the critical LESP value by spline interpolation of the calibrated data (Figure 5). If the absolute value of instantaneous LESP is higher than the critical LESP value, a vortex is shed from the leading edge. The strength of the vortex is calculated such that the LESP value is made equal to the critical LESP. The iteration procedure at each time step is summarized in Section II.F. Comparisons of flow topology and force coefficient data between the low-order model and CFD are presented for the same perching and hovering motions used to verify the LESP hypothesis in the previous section.

III.C.1.   Perching maneuvers

The three perching motions depicted in Figure 6 are used for validation of force and flow data from the theoretical model against CFD in this section. Figure 14 shows the variations of instantaneous LESP and critical LESP during the motion P1. The region where these curves coincide corresponds to vortices being shed from the leading edge. The $Re_{V_{mag}}$ variation is spiky because of LEV shedding constantly altering the velocity at the leading edge. These small spikes however do not significantly affect the critical LESP variation. Figure 15 shows the comparison in flow topology and Figure 16 shows the force data comparison for case P1.
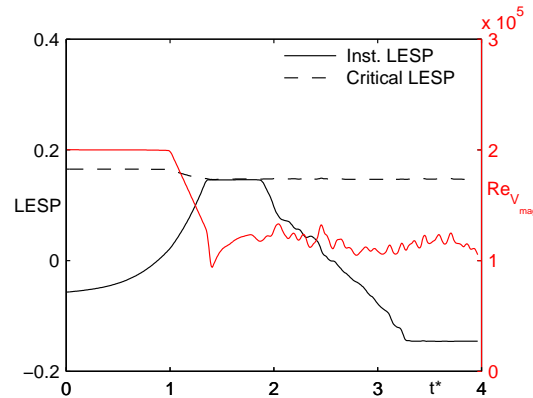

Figure 14. Case P1. Left axis: Instantaneous and critical LESP curves from theory. Right axis: Instantaneous $Re_{V_{mag}}$ value from which critical LESP is calculated using the calibration data.
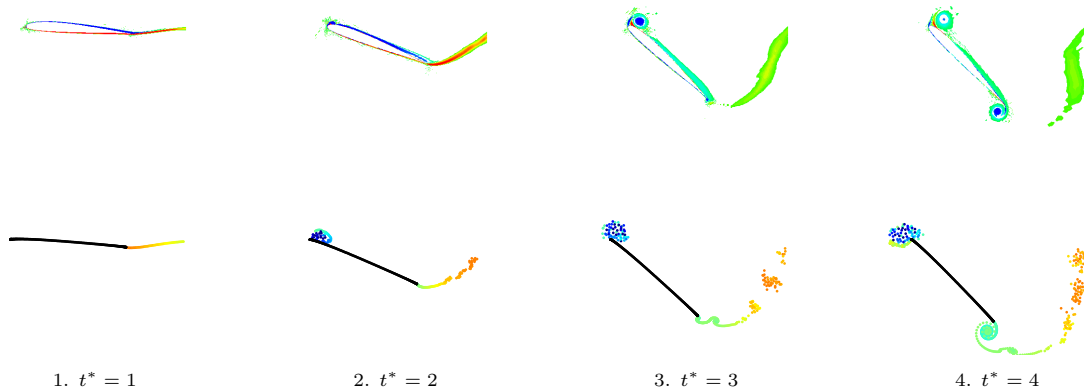

| 1. $t^* = 1$ | 2. $t^* = 2$ | 3. $t^* = 3$ | 4. $t^* = 4$ |

Figure 15. Case P1: Comparison of flow development figures from CFD and theory at four equally spaced intervals during the motion.
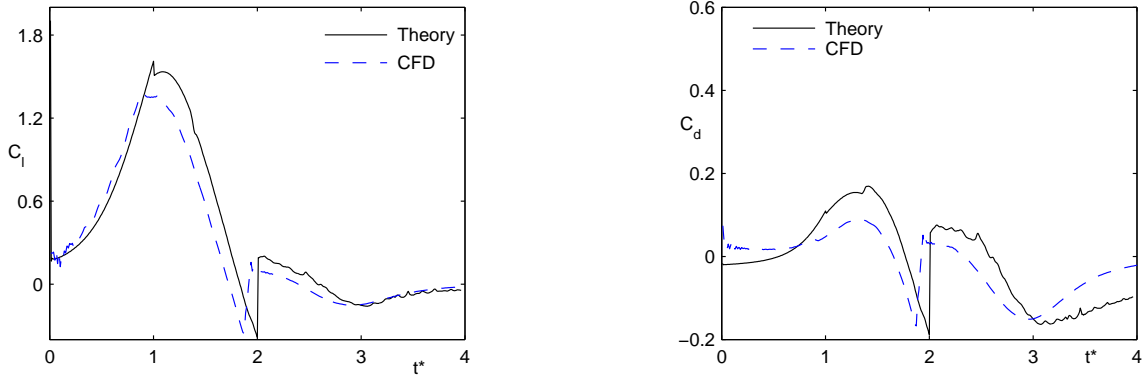
Figure 16. Case P1: Comparison of lift and drag coefficients from CFD and theory.

The variations of instantaneous LESP and critical LESP for the perching motion P2 are co-plotted in Figure 17. Figures 18 and 19 show the comparison between CFD and theory for flow and force data respectively.
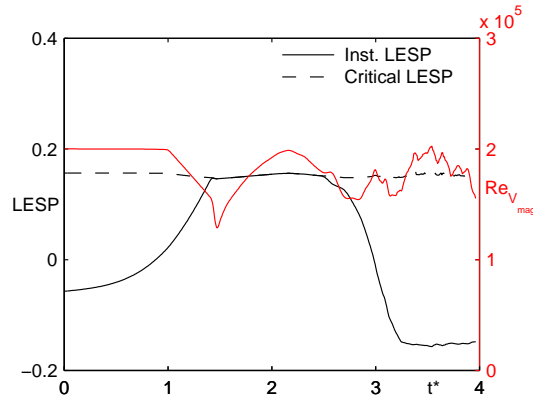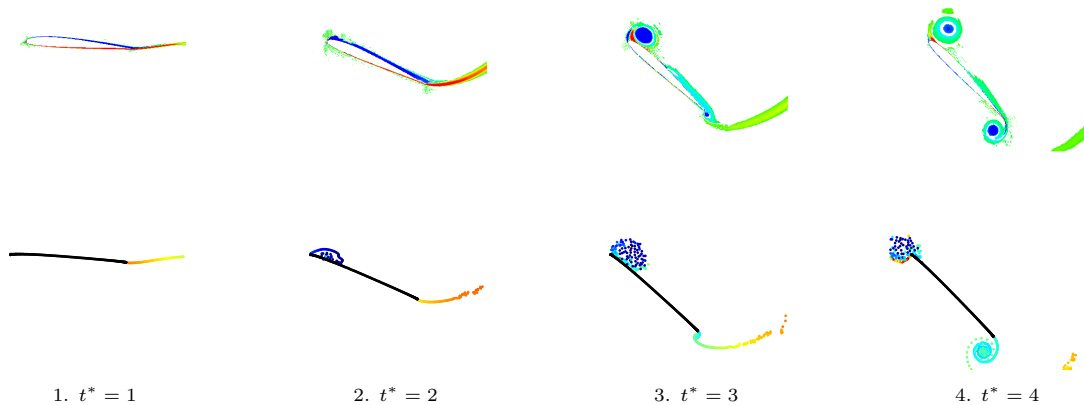

Figure 17. Case P2: Left axis: Instantaneous and critical LESP curves from theory. Right axis: Instantaneous $Re_{V_{mag}}$ value from which critical LESP is calculated using the calibration data.

1. $t^* = 1$ 2. $t^* = 2$ 3. $t^* = 3$ 4. $t^* = 4$

Figure 18. Case P2: Comparison of flow development figures from CFD and theory at four equally spaced intervals during the motion.

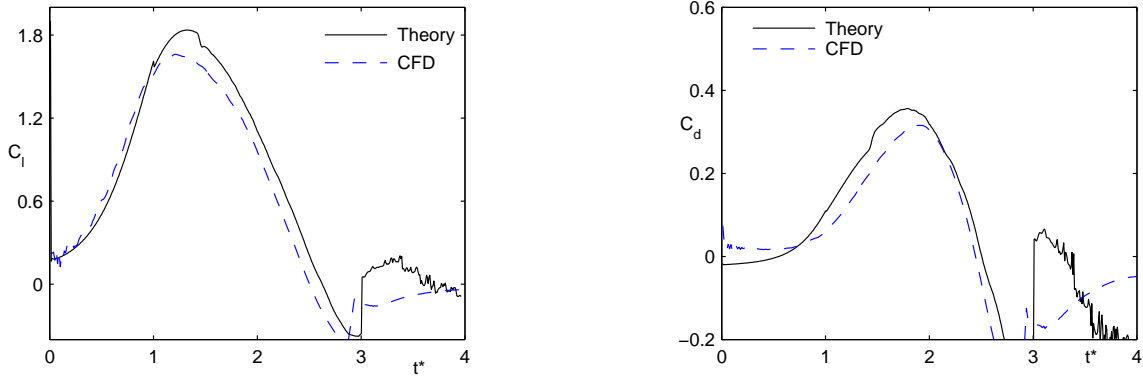American Institute of Aeronautics and Astronautics

Figure 19.   Case P2: Comparison of lift and drag coefficients from CFD and theory.

The variations of instantaneous LESP and critical LESP during the motion P3 are co-plotted in Figure 20. Figures 21 and 22 show the comparison between CFD and theory for flow and force data from case this case respectively.
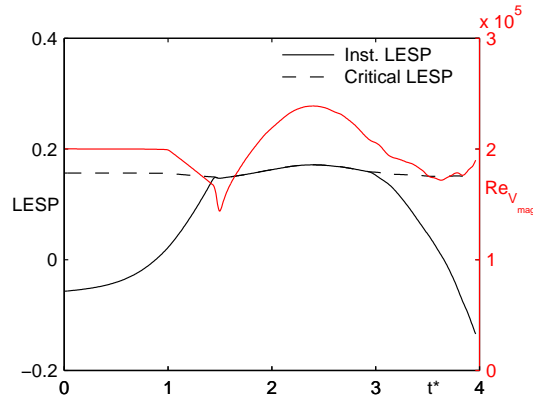

Figure 20.   Case P3. Left axis: Instantaneous and critical LESP curves from theory. Right axis: Instantaneous $Re_{V_{mag}}$ value from which critical LESP is calculated using the calibration data.

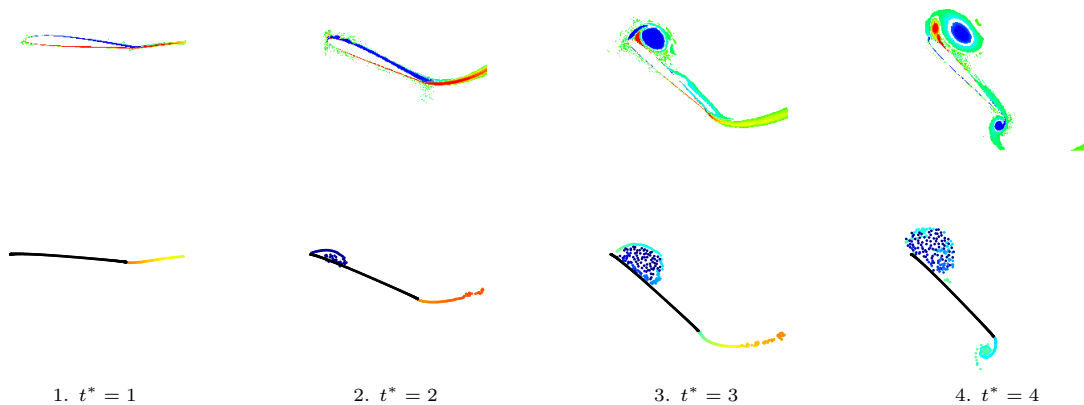1. $t^* = 1$ 2. $t^* = 2$ 3. $t^* = 3$ 4. $t^* = 4$

Figure 21.   Case P3: Comparison of flow development figures from CFD and theory at four equally spaced intervals during the motion.

In cases P1 and P2, flow topology from theory at the end of the motion (Figures 15 and 18) shows the
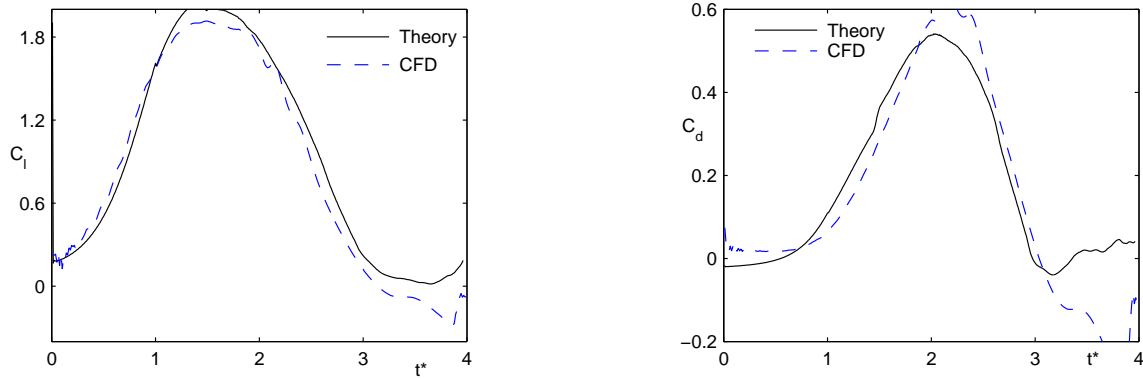
American Institute of Aeronautics and Astronautics

Figure 22. Case P3: Comparison of lift and drag coefficients from CFD and theory.

LEV tending to move over from the upper surface of the airfoil surface to the lower surface. This behavior is however not reflected in the CFD results. The error in the theoretical prediction may be attributed to the thin-airfoil theory approximation of neglecting airfoil thickness.

III.C.2. *Hovering maneuvers*

The three hovering motions depicted in Figure 10 are used for validation of force and flow data from the theoretical model against CFD in this section. The variations of instantaneous LESP and critical LESP for motion H1 are co-plotted in Figure 23. Again, we note that the region where these curves coincide corresponds to vortices being shed from the leading edge. Figure 24 shows the comparison in flow topology and Figure 25 shows the force data comparison for this case.
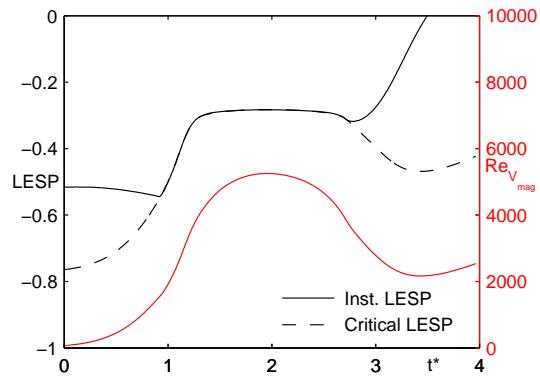
American Institute of Aeronautics and Astronautics

Figure 23. Case H1. Left axis: Instantaneous and critical LESP curves from theory. Right axis: Instantaneous $Re_{V_{mag}}$ value from which critical LESP is calculated using the calibration data.
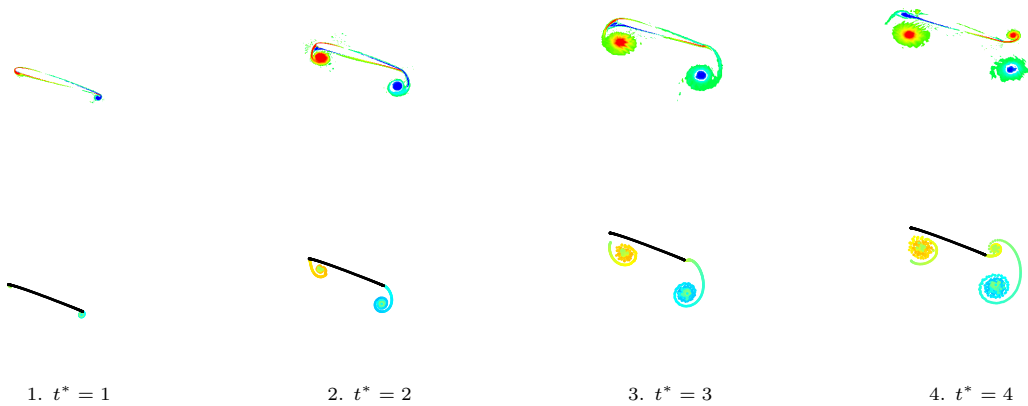

1. $t^* = 1$ 2. $t^* = 2$ 3. $t^* = 3$ 4. $t^* = 4$

Figure 24. Case H1: Comparison of flow development figures from CFD and theory at four equally spaced intervals during the motion.
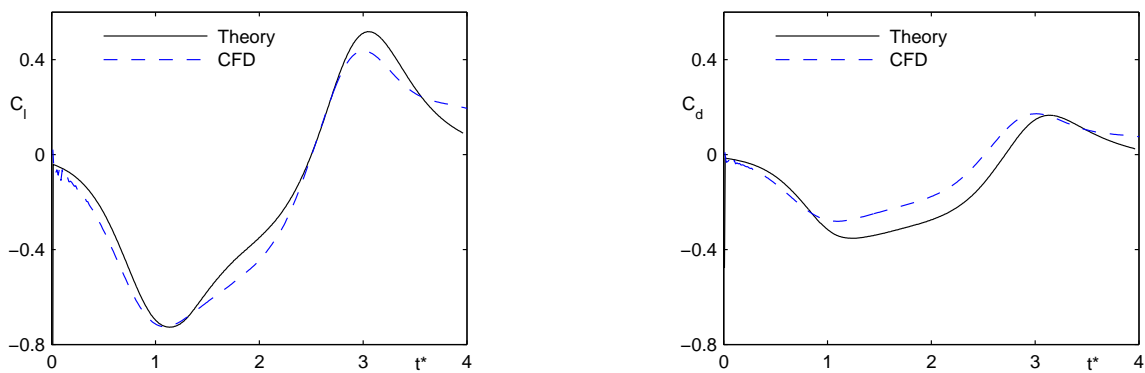

Figure 25. Case H1: Comparison of lift and drag coefficients from CFD and theory.

The variations of instantaneous LESP and critical LESP for case H2 are co-plotted in Figure 26. Figures 27 and 28 show the comparison between CFD and theory for flow and force data from case H2 respectively.
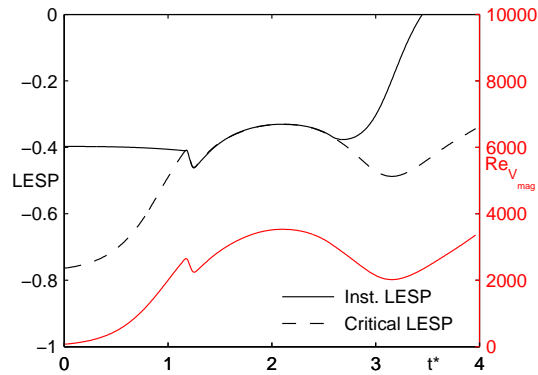

Figure 26. Case H2. Left axis: Instantaneous and critical LESP curves from theory. Right axis: Instantaneous $Re_{V_{mag}}$ value from which critical LESP is calculated using the calibration data.

| 1. $t^* = 1$ | 2. $t^* = 2$ | 3. $t^* = 3$ | 4. $t^* = 4$ |

Figure 27. Case H2: Comparison of flow development figures from CFD and theory at equally spaced intervals during the motion.

Figure 28. Case H2: Comparison of lift and drag coefficients from CFD and theory.

American Institute of Aeronautics and Astronautics

The variations of instantaneous LESP and critical LESP during the H3 motion are co-plotted in Figure 29. Figures 30 and 31 show the comparison between CFD and theory for flow and force data from this case.

Figure 29. Case H3. Left axis: Instantaneous and critical LESP curves from theory. Right axis: Instantaneous $Re_{V_{mag}}$ value from which critical LESP is calculated using the calibration data.
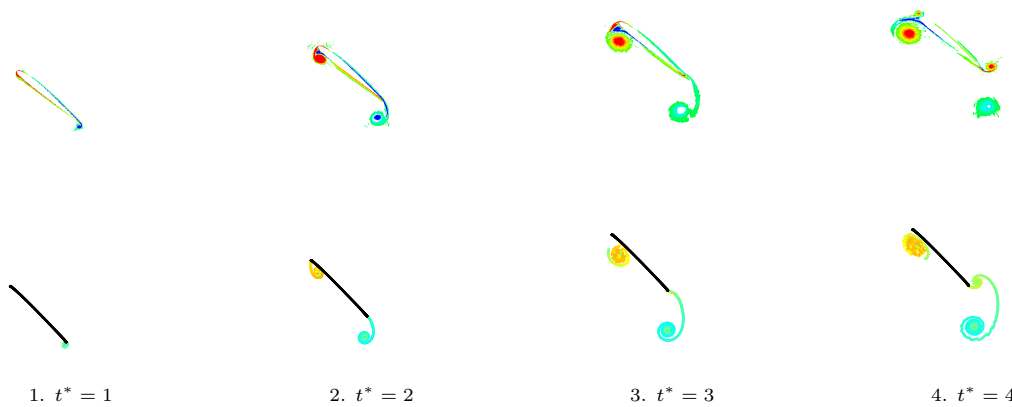

1. $t^* = 1$ 2. $t^* = 2$ 3. $t^* = 3$ 4. $t^* = 4$
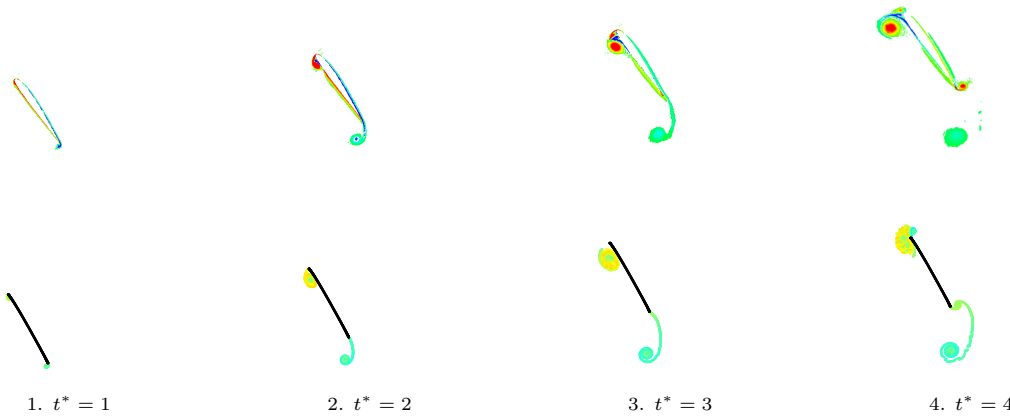
Figure 30. Case H3: Comparison of flow development figures from CFD and theory at equally spaced intervals during the motion.

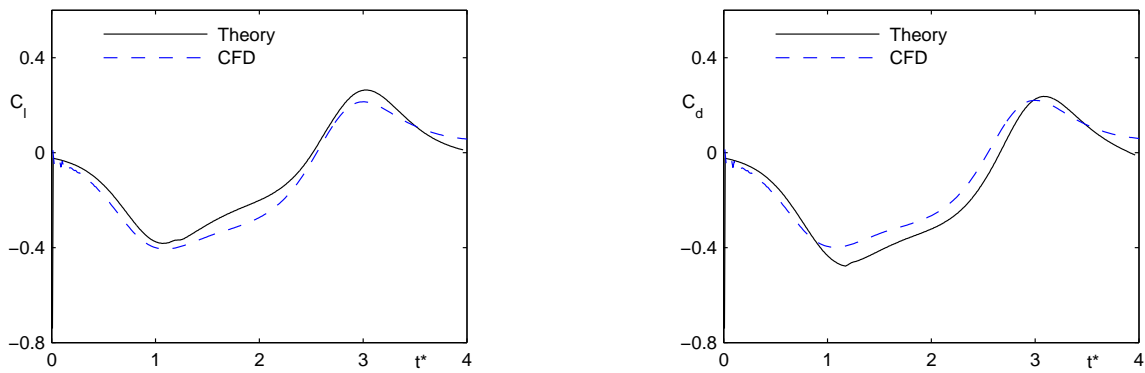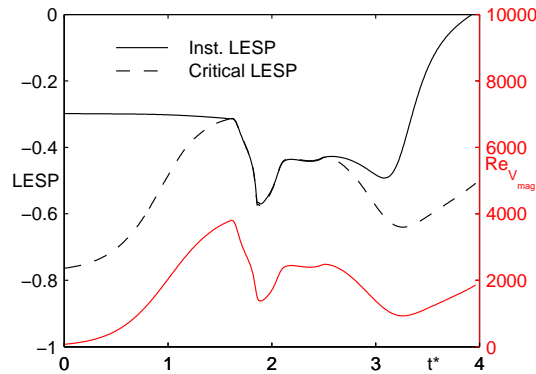Figure 31. Case H3: Comparison of lift and drag coefficients from CFD and theory.

It is reasonable to assume that some error was introduced in the solution because of splining the $LESP_{crit}$ curve over a large range of Reynolds numbers with few data points. It is expected that acquiring a calibration

American Institute of Aeronautics and Astronautics

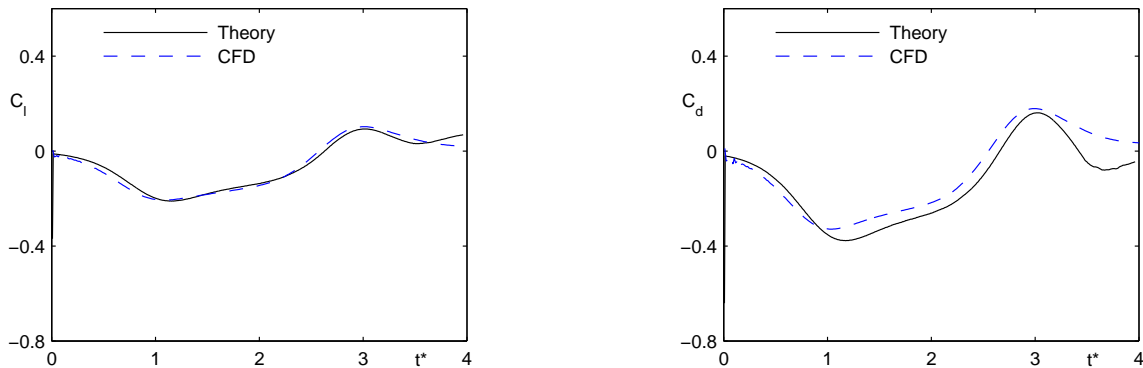curve with more data points would increase the accuracy of the solution.

IV.   Conclusions

Comparison of flow topology and force histories between the low-order model and CFD evinced considerable success of the former in modeling unsteady flows in which the freestream/translational velocity was either zero or small compared to motion and vortex-induced contributions. An important outcome of this effort is the recognition of the need to use a Reynolds number that is based on the velocity magnitude at the leading edge. The use of this $Re_{V_{mag}}$ results in a variation of the critical LESP during such motions. LEV formation corresponded with the LESP value exceeding $LESP_{crit}$ value at the instantaneous $Re_{V_{mag}}$. LEV shedding was modeled using point vortices and the strength of the shed vortices were determined through iteration such that the LESP is brought back to the critical value. This condition was used rather than a Kutta condition in order to model rounded leading edges more accurately, which can support some suction even when flow is separated. Good comparison of force data from the low-order model against CFD provides support in favor of this hypothesis. Typical run-times for this method were between 30 and 40 seconds, enabling it to be a fast tool for use in simulation, control and design.

V.   Acknowledgments

References

[1] Jardin, T., David, L., and Farcy, A., "Characterization of Vortical Structures and Loads Based on Time-resolved PIV for Asymmetric Hovering Flapping Flight," *Experiments in fluids*, Vol. 46, No. 5, 2009, pp. 847–857.

[2] Kurtulus, D. F., David, L., Farcy, A., and Alemdaroglu, N., "Aerodynamic Characteristics of Flapping Motion in Hover," *Experiments in fluids*, Vol. 44, No. 1, 2008, pp. 23–36.

[3] Viieru, J. T. D. and Shyy, W., "Effects of Reynolds Number and Flapping Kinematics on Hovering Aerodynamics," AIAA Paper 2007-0129, 2007.

[4] Berman, G. and Wang, Z., "Energy-minimizing Kinematics in Hovering Insect Flight," *Journal of Fluid Mechanics*, Vol. 582, No. 1, 2007, pp. 153–168.

[5] Granlund, K., Ol, M. V., Visbal, M., and Bernal, L., "Experiments and Computations on Abstraction of Perching," AIAA Paper 2010-4943, 2010.

[6] Theodorsen, T., "General Theory of Aerodynamic Instability and the Mechanism of Flutter," NACA Rept. 496, 1935.

[7] Wagner, H., "Über die Entstehung des dynamischen Auftriebes von Tragflügeln," *ZaMM*, Vol. 5, No. 1, 1925, pp. 17–35.

[8] von Kármán, T. and Sears, W., "Airfoil Theory for Non-Uniform Motion," *Journal of the Aeronautical Sciences*, Vol. 5, No. 10, August 1938, pp. 379–390.

[9] Isaacs, R., "Airfoil Theory for Flows of Variable Velocity," *Journal of the Aeronautical Sciences*, Vol. 12, No. 1, 1945, pp. 113–117.

[10] Greenberg, J. M., "Airfoil in Sinusoidal Motion in a Pulsating Stream," NACA Report TN-1326, 1947.

[11] van der Wall, B. and Leishman, J., "On the influence of time-varying flow velocity on unsteady aerodynamics," *Journal of the American Helicopter Society*, Vol. 39, No. 4, 1994, pp. 25–36.

[12] Leishman, J. G., *Principles of Helicopter Aerodynamics*, Cambridge Aerospace Series, Cambridge University Press, Cambridge, 2002.

[13] Ellington, C., Van Den Berg, C., Willmott, A., and Thomas, A., "Leading-edge vortices in insect flight," *Nature*, Vol. 384, 1996, pp. 626–630.

[14] Shyy, W. and Liu, H., "Flapping Wings and Aerodynamic Lift: The Role of Leading-Edge Vortices," *AIAA journal*, Vol. 45, No. 12, 2007.

[15] Ellington, C., "The novel aerodynamics of insect flight: applications to micro-air vehicles," *Journal of Experimental Biology*, Vol. 202, No. 23, 1999, pp. 3439–3448.

[16] Dickinson, M. and Gotz, K., "Unsteady aerodynamic performance of model wings at low Reynolds numbers," *Journal of Experimental Biology*, Vol. 174, No. 1, 1993, pp. 45–64.

[17] Sarpkaya, T., "An inviscid model of two-dimensional vortex shedding for transient and asymptotically steady separated flow over an inclined plate," *Journal of Fluid Mechanics*, Vol. 68, No. 01, 1975, pp. 109–128.

[18] Katz, J., "Discrete Vortex Method for the Non-Steady Separated Flow Over an Airfoil," *Journal of Fluid Mechanics*, Vol. 102, 1981, pp. 315–328.

[19] Clements, R., "An inviscid model of two-dimensional vortex shedding," *J. Fluid Mech*, Vol. 57, No. 2, 1973, pp. 321–336.

[20] Leonard, A., "Vortex methods for flow simulation," *Journal of Computational Physics*, Vol. 37, No. 3, 1980, pp. 289–335.

[21]Ansari, S., Żbikowski, R., and Knowles, K., "Non-linear unsteady aerodynamic model for insect-like flapping wings in the hover. Part 1: methodology and analysis," *Proceedings of the Institution of Mechanical Engineers, Part G: Journal of Aerospace Engineering*, Vol. 220, No. 2, 2006, pp. 61–83.

[22]Pullin, D. and Wang, Z. J., "Unsteady forces on an accelerating plate and application to hovering insect flight," *Journal of Fluid Mechanics*, Vol. 509, 2004, pp. 1–21.

[23]Wang, C. and Eldredge, J., "Low-order phenomenological modeling of leading-edge vortex formation," *Theoretical and Computational Fluid Dynamics*, 2012, DOI: 10.1007/s00162-012-0279-5.

[24]Hemati, M. S., Eldredge, J. D., and Speyer, J. L., "Improving Vortex Models via Optimum Control Theory," AIAA Paper 2013–0351, 2013.

[25]Ramesh, K., Gopalarathnam, A., Edwards, J. R., Ol, M. V., and Granlund, K., "An Unsteady Airfoil Theory Applied to Pitching Motions Validated Against Experiment and Computation," *Theoretical and Computational Fluid Dynamics*, 2012, DOI: 10.1007/s00162-012-0292-8.

[26]Ramesh, K., Gopalarathnam, A., Ol, M. V., Granlund, K., and Edwards, J. R., "Augmentation of Inviscid Airfoil Theory to Predict and Model 2D Unsteady Vortex Dominated Flows," AIAA Paper 2011–3578, 2011, Revised version in review for publication in AIAA Journal.

[27]Ramesh, K., Gopalarathnam, A., Granlund, K., Ol, M. V., and Edwards, J. R., "Theoretical Modeling of Leading Edge Vortices Using the Leading Edge Suction Parameter," AIAA Paper 2012–3027, 2012.

[28]Katz, J. and Plotkin, A., *Low-Speed Aerodynamics*, Cambridge Aerospace Series, 2000.

[29]Garrick, I., "Propulsion of a Flapping and Oscillating Airfoil," NACA Rept. 567, 1937.

[30]von Kármán, T. and Burgers, J., *General Aerodynamic Theory - Perfect Fluids*, Vol. 2 of Aerodynamic theory: a general review of progress, Durand, W. F. , Dover Publications, 1963.

[31]Evans, W. T. and Mort, K. W., "Analysis of Computed Flow Parameters for a set of Sudden Stalls in Low Speed Two-Dimensional Flow," NACA Report TND-85, 1959.

[32]T.S.Beddoes, "Onset of Leading Edge Separation Effects under Dynamic Conditions and Low Mach Number," 34th Annual forum of the American Helicopter Society, 1978.

[33]Ansari, S., Żbikowski, R., and Knowles, K., "Non-linear unsteady aerodynamic model for insect-like flapping wings in the hover. Part 2: implementation and validation," *Proceedings of the Institution of Mechanical Engineers, Part G: Journal of Aerospace Engineering*, Vol. 220, No. 3, 2006, pp. 169–186.

[34]Vatistas, G., Kozel, V., and Mih, W., "A simpler model for concentrated vortices," *Experiments in Fluids*, Vol. 11, No. 1, 1991, pp. 73–76.

[35]Cassidy, D. A., Edwards, J. R., and Tian, M., "An Investigation of Interface-Sharpening Schemes for Multiphase Mixture Flows," *Journal of Computational Physics*, Vol. 228, No. 16, 2009, pp. 5628–5649.

[36]Spalart, P. R. and Allmaras, S. R., "A One-Equation Turbulence Model for Aerodynamic Flows," AIAA Paper 92–0439, 1992.

[37]Edwards, J. R. and Chandra, S., "Comparison of Eddy Viscosity - Transport Turbulence Models for Three-Dimensional, Shock-Separated Flowfields," *AIAA Journal*, Vol. 34, No. 4, 1996, pp. 756–763.

[38]Ramesh, K., Ke, J., Gopalarathnam, A., and Edwards, J. R., "Effect of Airfoil Shape and Reynolds Number on Leading Edge Vortex Shedding in Unsteady Flows," AIAA Paper 2012–3025, 2012.

Appendices

A. Identification of LEV formation from CFD

The surface skin friction (C_f) distributions from CFD provide a quantitative method of identifying the onset of LEV formation. LEV formation is preceded by the formation of a small region of reversed flow (negative vorticity) near the leading edge of the airfoil. Onset of LEV shedding is subsequently initiated by the formation of a shear layer at the leading edge and this is accompanied by the development of a small region of positive vorticity, adjacent to the region of negative vorticity described earlier. Thus the formation of alternating positive and negative vorticity near the leading edge is a useful signature which we will use to determine the exact instant when LEV formation begins. Since the process of identifying onset of LEV formation visually using the vorticity plots is qualitative, we translate the same criterion to the skin friction coefficient. The formation of a negative vorticity region near the leading edge is indicated by a negative skin friction coefficient near the leading edge. The formation of the positive vorticity region, which accompanies the development of the shear layer can be identified by alternating positive and negative spikes in the skin fiction coefficient. Figure 32 shows a series of vorticity and skin friction coefficient plots for an airfoil undergoing leading edge separation.
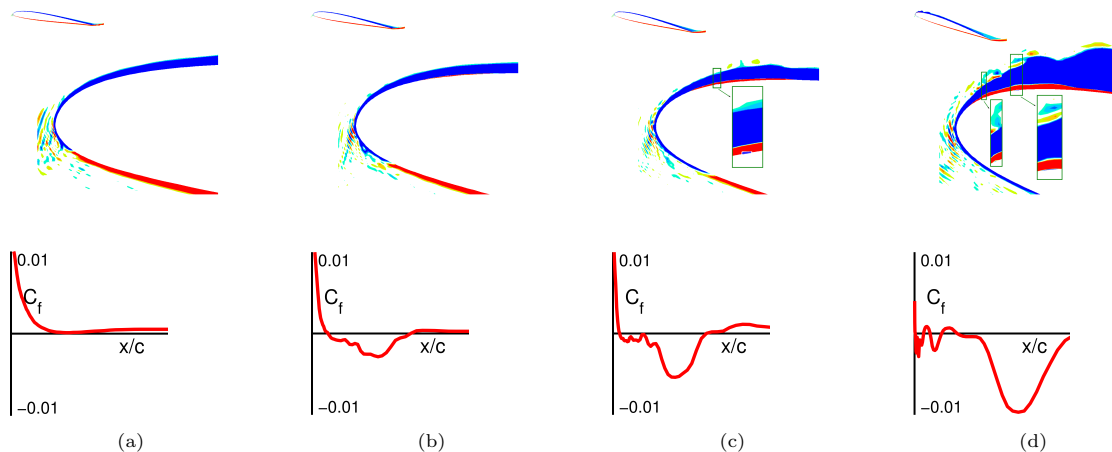

Figure 32. Vorticity and skin friction coefficient plots from CFD during the LEV formation process. Appearance of positive vorticity region is circled.

The flow phenomena at instants (a) through (d) in the figure are described below:

- (a) The flow is attached at the leading edge.

- (b) The boundary layer is still attached. However, there is a region of reversed flow near the leading edge, reflected in both the vorticity plot and the skin friction coefficient.

- (c) Start of formation of the shear layer. A small region of positive vorticity starts developing adjacent to the negative vorticity at the leading edge. This also corresponds to the start of formation of alternating spikes in the skin friction coefficient near the leading edge. We use this signature in the C_f to identify the start of LEV formation in all results from CFD.

- (d) Shear layer is well established and LEV shedding is in progress.